

Radiation detection using fully depleted 50 μm thick Ni/n-4H-SiC epitaxial layer Schottky diodes with ultra-low concentration of $\text{Z}_{1/2}$ and $\text{EH}_{6/7}$ deep defects

Cite as: J. Appl. Phys. 128, 114501 (2020); doi: 10.1063/5.0021403

Submitted: 10 July 2020 · Accepted: 1 September 2020 ·

Published Online: 18 September 2020



View Online



Export Citation



CrossMark

Sandeep K. Chaudhuri, Joshua W. Kleppinger, and Krishna C. Mandal^{a)}

AFFILIATIONS

Department of Electrical Engineering, University of South Carolina, Columbia, South Carolina 29208, USA

^{a)}Author to whom correspondence should be addressed: mandalk@cec.sc.edu. Tel.: +1 (803) 777-2722

ABSTRACT

Recent advances in the development of thick 4H-SiC epitaxial layers for the fabrication of surface barrier radiation detectors have been paving the way for their use in highly penetrating radiation detection. Challenges still exist to achieve full depletion all the way to the epilayer width, while maintaining a low leakage current at high reverse bias conditions. We report the fabrication of high-resolution and low leakage current Schottky barrier alpha particle detectors with a large active area of 11 mm² on 50 μm thick n-type 4H-SiC epitaxial layers, which can be fully depleted. The detectors were cut out of large substrates of 100 mm diameter with a micropipe density $<1\text{ cm}^{-2}$ in the epilayers. Mott-Schottky plots obtained from the capacitance-voltage measurements revealed an effective doping concentration of $1.9 \times 10^{14}\text{ cm}^{-3}$. A parallel plate capacitor model implied that a reverse bias of $\sim 440\text{ V}$ was needed to achieve a full-depletion width (50 μm). The current-voltage characteristics demonstrated a very low leakage current of 0.45 nA at a reverse bias of -450 V , which is low enough for the detector to be operated at full-depletion bias. In fact, pulse height spectroscopy using a ²⁴¹Am alpha source, with the detector biased at -120 V , exhibited a well-resolved alpha spectrum with an energy resolution of 0.8% for the alpha peak corresponding to 5486 keV. This energy resolution was maintained consistently up to a full-depletion bias of -440 V . The ultra-stable performance of the detector has been attributed to the remarkably low concentration of carrier lifetime affecting deep-level defects like $\text{Z}_{1/2}$ and $\text{EH}_{6/7}$, which were found to be of the order of 10^{12} cm^{-3} or less using capacitance mode deep-level transient spectroscopy measurements.

Published under license by AIP Publishing. <https://doi.org/10.1063/5.0021403>

I. INTRODUCTION

Epitaxially grown 4H-SiC, a polytype of silicon carbide (SiC), has established itself as a next-generation material for fabrication of high-resolution detectors for ionizing nuclear radiation.^{1–8} Because of its high threshold displacement energy (19 eV for C and 42 eV for Si),⁹ 4H-SiC is a radiation hard material. It is also highly chemically inert and has an extremely high melting point. These properties make 4H-SiC devices operable at harsh environments like space missions, nuclear core reactors, accelerator environments, and in laser generated plasma environments as in facilities for high-energy particle generation.^{10–13}

4H-SiC epitaxial layer Schottky barrier diodes (SBDs) have established themselves as alpha particle detectors with high-energy

resolution.^{14,15} Apart from charged particle detection, 4H-SiC has been reported to be also highly sensitive to soft x-rays of energy up to 50 eV and has achieved high-energy resolution of 2.1% for 59.6 keV gamma rays.^{16–18} Bulk semi-insulating 4H-SiC could have been a better choice in terms of absorption of highly penetrating gamma rays but presently available crystal quality is inadequate for radiation detection.^{17,19} Epitaxial 4H-SiC layers, on the other hand, can be grown as highly crystalline detector-grade semiconductor materials. Radiation detectors with thicker epitaxial layers are being reported offering better x/ γ -photon³ and neutron¹¹—absorption.

Mere production of SBDs on thicker epitaxial layers will not suffice the purpose of efficient detection of highly penetrating radiation unless the SBDs are fully depleted with widths equaling the epilayer thickness. Full-depletion width requires high operating bias

conditions where the leakage currents could be too high to maintain low noise conditions. Recently, Puglisi and Bertuccio have reported the fabrication of fully depleted position sensitive microstrip x-ray detectors on $124\text{ }\mu\text{m}$ thick epitaxial 4H-SiC with 32 strips fabricated on a detector area of $3.35 \times 2\text{ mm}^2$.³ In this article, we report the fabrication of fully depleted alpha detectors on epitaxially grown 4H-SiC layers with thickness up to $50\text{ }\mu\text{m}$ and electrode area of 0.11 cm^2 . The $8 \times 8\text{ cm}^2$ detector wafers were cut from parent wafers of diameter 100 mm with a micropipe density less than 1 cm^{-2} . Micropipes²⁰ are hollow-core threading screw dislocations (TSDs), which are known to induce device failures and reliability issues.^{21,22} TSDs are one of the three structural defects that preexist in the 4H-SiC substrate and can propagate to the epitaxial layers. Micropipes can also dissociate at the substrate-epilayer interface to multiple closed-core TSDs, which are believed to be responsible for premature breakdown in 4H-SiC based power devices.²³ The other two defect categories that propagate from the substrate to the epitaxial layer are threading edge dislocations (TEDs) and basal plane dislocations (BPDs). TEDs are believed to be benign in comparison to TSDs and BPDs.²² BPDs normally transform into benign TEDs during epitaxial layer growth but can also propagate through and can cause V_f drift in bipolar devices.²⁴ With the substantial reduction in the micropipe density, the performance of the 4H-SiC radiation detectors reported in this work is expected to be mostly limited by the presence of deep-level point defects that can act as potential trapping and recombination centers.^{25–28}

We describe the fabrication and characterization of high-resolution n-type 4H-SiC epitaxial layer alpha particle detectors and the nature of point defects that can affect the performance of these devices. Deep-level transient spectroscopy (DLTS) in the capacitance mode has been used to study the electron trapping centers by calculating their locations within the bandgap, their

concentration, and capture cross sections. The detector performance was evaluated using pulse height spectroscopy with a ^{241}Am alpha emitting source at different bias voltages including full-depletion bias.

II. EXPERIMENTAL METHODS

A. Detector fabrication

$50\text{ }\mu\text{m}$ thick n-type 4H-SiC epitaxial layers were grown on the (0001) Si face of a $350\text{ }\mu\text{m}$ thick 4H-SiC substrates with a diameter of 100 mm. The substrates were 8° offcut toward the $\langle 11\bar{2}0 \rangle$ direction to facilitate step-controlled epitaxial growth, which in turn helps reduce the surface defects.²⁹ A schematic of the crystal faces and the direction convention has been explained in Fig. 1(a). Figure 1(b) illustrates the construction of the epilayer detector with the physical dimensions. The $8 \times 8\text{ mm}^2$ wafers were diced out from the parent wafers and cleaned following the RCA wafer cleaning procedure.³⁰ The native oxide layers were dissolved using concentrated hydrofluoric acid prior to contact deposition. The $50\text{ }\mu\text{m}$ thick epilayer on the top is the active device layer on which 20 nm thick circular (diameter $\sim 3.8\text{ mm}$) nickel contacts were deposited using a Quorum Q150T sputter coater. Thin nickel contacts are necessary to reduce energy loss of the incident radiation through scattering.³¹ The thin Ni contacts formed Schottky barrier diodes (SBDs) with the depletion region extending to the epilayer. A reverse bias condition was obtained when this contact (anode) is at negative potential with respect to the thicker bottom Ni contact. The bottom contacts (cathode) were square shaped ($6 \times 6\text{ mm}^2$) sputter coated nickel with a thickness of 100 nm . For establishing electrical connections with the metal contacts, the detectors were mounted on printed circuit boards (PCBs) with a metal pad forming the cathode connection. For the anode connection, $25\text{ }\mu\text{m}$ thin gold wires were wire bonded using highly conducting silver

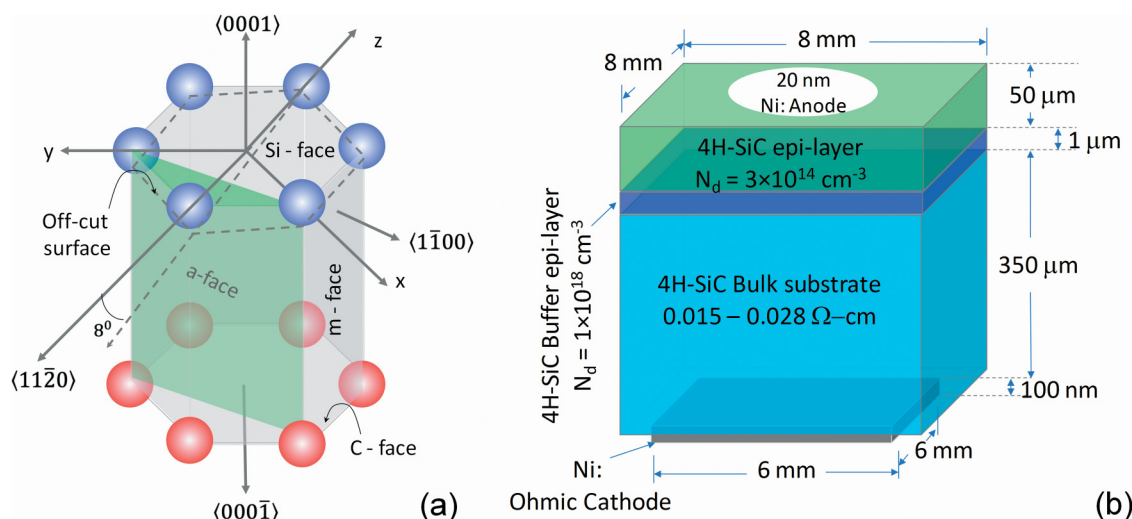


FIG. 1. (a) Schematic showing the crystal planes and crystallographic directions in the 4H-SiC polytype. The dotted hexagon shows the offcut plane in the substrates. (b) Illustration of the construction of Ni/n-4H-SiC $50\text{ }\mu\text{m}$ epitaxial layer detectors. The $\sim 1\text{ }\mu\text{m}$ thick buffer layer helps reduce the propagation of the TSDs, TEDs, and BPDs.

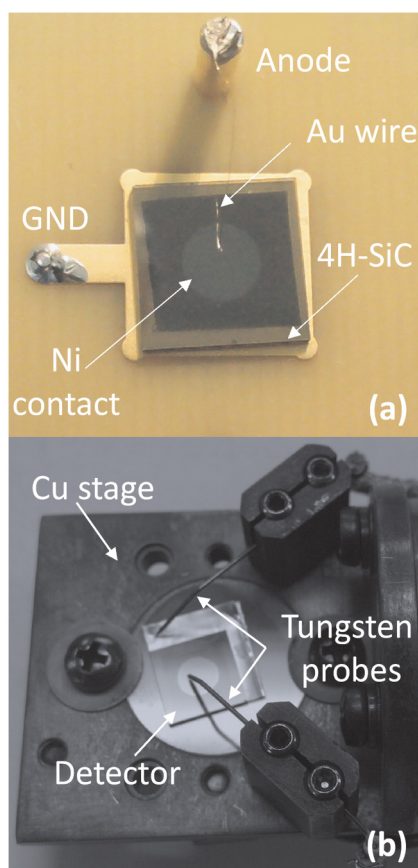


FIG. 2. (a) Photograph of a 4H-SiC SBD mounted on a PCB with the Ni anode bonded using a $25\ \mu\text{m}$ Au wire. (b) A bare detector mounted on the copper stage of a VPF-800 JANIS cryostat electrically connected using tungsten microprobes for DLTS measurements.

epoxy. The other end of the gold wire was attached to another pad on the PCB forming the anode connection. Figure 2(a) shows such a detector in its finished form.

B. Detector characterization

The detectors were characterized for the Schottky barrier properties using current–voltage (I – V) and capacitance–voltage (C – V) measurements. A Keithley 237 source-meter unit was used to record the I – V characteristics. The detectors were placed in an electromagnetic interference (EMI) shielded box during the measurements, which was equipped with BNC and triax connectors for connecting to the low noise coaxial cables. The connectors were soldered to the detector PCB for secure electrical connections. The C – V measurements were carried out at 1 MHz test frequency using a SULA DLTS equipment, which will be described in Sec. II C.

The detection properties of the detectors were evaluated using a pulse height spectrometer. The spectrometer was connected to an EMI shielded test box equipped with coaxial connectors and a

vacuum port. The test box was continuously evacuated using a vacuum pump during the alpha particle measurements to eliminate the scattering of alpha particles by air molecules. The spectrometer comprised of an Amptek A250CF charge-sensitive preamplifier that integrates the detector current to produce a voltage output directly proportional to the amount of charge induced in the detector due to the incident ionizing radiation. The preamplifier output was filtered using an ORTEC 572 spectroscopy amplifier. The semi-Gaussian shaped pulses were digitized using a Canberra Multiport II multichannel analyzer (MCA), which also produced histograms or pulse height spectra (PHS). A $0.9\ \mu\text{Ci}$ ^{241}Am radioisotope emitting primarily 5486 keV, 5443 keV, and 5388 keV alpha particles was used to obtain the PHS. The interactions of the alpha particles manifests as peaks in the PHS. To determine the energy resolution of the detection system, the peaks were fitted with Gaussian functions to obtain the width of the peaks in terms of the full width at half maximum ($FWHM$). The $FWHM$ of the alpha peak expressed as the percentage of the actual energy of the detected peak was defined as the percentage energy resolution of the detector at that radiation source energy.

C. Deep-level transient spectroscopy (DLTS)

The DLTS measurements were carried out using a SULA DDS-12 modular DLTS system. The DLTS system comprised of a pulse generator module for applying repetitive bias pulse, a 1 MHz oscillator for capacitance measurements, a sensitive capacitance meter involving a self-balancing bridge circuit, and a correlator/preamplifier module that automatically removes DC background from the capacitance meter and amplifies the resultant signal change. The correlation was based on a modified double boxcar signal averaging system. The sample in its bare form (without the PCB and wire bonds) was mounted on a copper stage with tungsten microprobes for electrical connections in a Janis VPF 800 LN_2 cryostat. The arrangement is shown in Fig. 2(b). The temperature variation of the sample stage was controlled by a Lakeshore LS335 temperature controller. The DDS-12 system allows the user to collect four DLTS spectra simultaneously with four different correlator delay settings in a single temperature scan. All the signals were digitized using a National Instruments (NI) digitizer card integrated with the DLTS system for online processing using a PC. The entire system including the modules and the temperature controller is controlled using a dedicated LabVIEW interface, which also allows the user to analyze the recorded data.

III. RESULTS

A. Electrical characterization

Figure 3 shows the I – V characteristic of a $50\ \mu\text{m}$ thick Ni/n-4H-SiC epitaxial Schottky barrier diodes. The characteristic confirms the rectifying behavior of the Ni–4H-SiC interface. The detector behaved as reverse biased with a negative polarity bias applied to the top circular contact (anode). A leakage current of $0.45\ \text{nA}$ ($4.09\ \text{nA}/\text{cm}^2$) was observed at a reverse bias of $-450\ \text{V}$. It could be noted that 4H-SiC detectors with lower leakage current density from a few pA/cm^2 to $0.3\ \text{nA}/\text{cm}^2$ have been reported

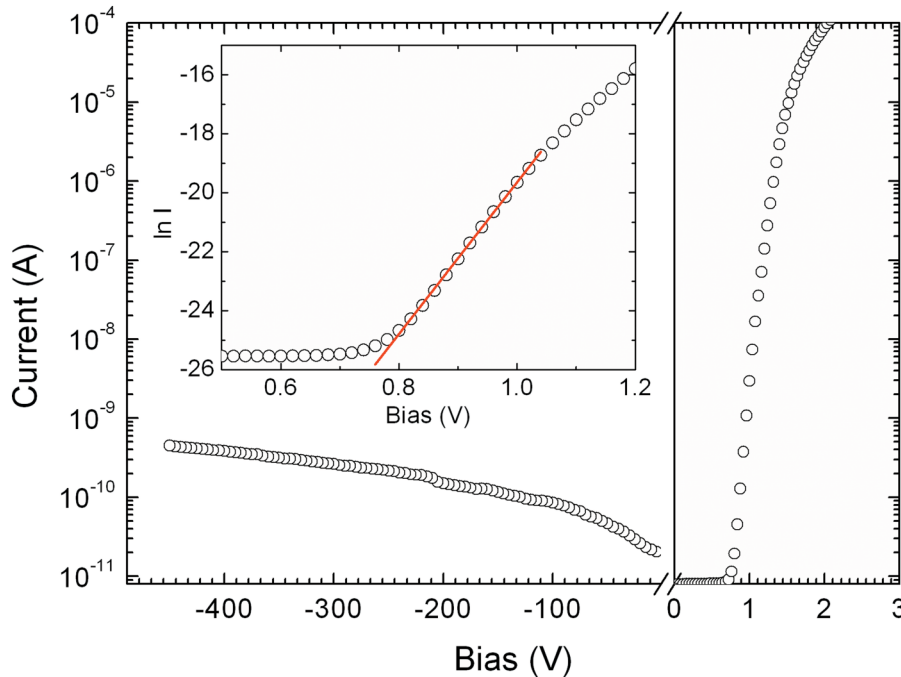


FIG. 3. Reverse and forward diode current plotted as a function of bias voltage for a Ni/n-4H-SiC Schottky barrier diode. The inset shows the corresponding $\ln I$ - V plot with the solid line as the linear fit of a thermionic emission model to the experimental data points.

earlier.^{32,33} The obtained leakage current for the present detector is although higher than those reported in silicon p-n junction³⁴ diodes and comparable to CdTe Schottky junction diodes,³⁵ the magnitude of electric field that the present detectors sustain (~ 90 kV/cm) at the operating bias of -450 V is much higher than those sustained by Si and CdTe diodes. Low leakage currents together with detector capacitance does define the electronic noise of radiation detectors, however, for alpha particle spectroscopy and high junction capacitance a leakage current even of magnitude 1 nA at the operating bias is not much of a concern. The observed high leakage current can nevertheless be lowered by inclusion of guard ring structure in the detector design.

The forward I - V characteristic can offer lot of useful information when assumed to follow theoretical models. A thermionic emission model of SBD^{36,37} predicts the variation of forward diode current I_F as a function of forward bias V_F as given in Eq. (1),

$$I_F = A^{**} AT^2 e^{-q\phi_{b0}/kT} e^{-q\beta V_F/kT} \left\{ e^{\frac{qV_F}{kT}} - 1 \right\}, \quad (1)$$

where A^{**} is the effective Richardson constant ($146 \text{ A cm}^2 \text{ K}^2$ for 4H-SiC), A is the effective contact area participating in current flow, T is the absolute junction temperature, q is the electronic charge, ϕ_{b0} is the zero bias barrier height, k is the Boltzmann constant, and $\beta = \frac{\partial \phi_b}{\partial V_F}$ gives the variation of the barrier height ϕ_b with bias voltage. The barrier height could vary with the forward bias due to any change in voltage drop across the interfacial layer or due to the change in image force with the applied bias. The factor β is related to the diode ideality factor n as $\frac{1}{n} = 1 - \beta$. For values of $V_F > 3 kT/q$, Eq. (1) can be modified as

$$I_F = A^{**} AT^2 e^{-q\phi_{b0}/kT} e^{-qV_F/nkT}. \quad (2)$$

The experimentally measured I - V characteristics in the fabricated Ni/n-4H-SiC diode were fitted according to Eq. (2). A straight line fit of the $\ln I_F$ - V_F plot as shown in the inset of Fig. 3 obtained a barrier height of 1.54 eV and a diode ideality factor of 1.5 . A β value of 0.33 was calculated using the above model.

Further information on the current (reverse) flow mechanism can be obtained from the variation of reverse leakage current I_R , as a function of the applied electric field.^{38,39} Lowering of barrier in the junction depletion region due to Schottky lowering mechanism is given by

$$I_R \propto T^2 \exp\left(\frac{q}{2kT} \sqrt{\frac{qE}{\pi\epsilon_0\epsilon_{4H-SiC}}}\right), \quad (3)$$

where E is the applied electric field calculated as the ratio of the applied reverse bias to the thickness of the epilayer, ϵ_0 is the permittivity of free space, ϵ_{4H-SiC} ($=9.7$) is the dielectric constant of 4H-SiC. On the other hand, the lowering of barrier height due to Poole-Frenkel effect (PFE) is given by

$$I_R \propto E \exp\left(\frac{q}{kT} \sqrt{\frac{qE}{\pi\epsilon_0\epsilon_{4H-SiC}}}\right), \quad (4)$$

The mechanism of lowering of barrier height can be identified from the slopes of linear fit to the $\ln I_R/E - E^{1/2}$ or $\ln I_R/T^2 - E^{1/2}$ plots. The two slopes are given by

$$S = \frac{q}{mkT} \sqrt{\frac{q}{\pi \epsilon_0 \epsilon_{4H-SiC}}}, \quad (5)$$

where $m = 1$ for Poole–Frenkel type lowering and $m = 2$ for Schottky type lowering. The theoretical values of the slopes at 300 K are calculated using Eq. (5) to be 0.006 and 0.02 for $m = 1$ and $m = 2$, respectively. Figures 4(a) and 4(b) show the $\ln I_R/E - E^{1/2}$ and $\ln I_R/T^2 - E^{1/2}$ plots along with the linear fit, respectively. The slope of the Schottky type emission plot was found to be 0.0047 and that of the Poole–Frenkel type was found to be 0.009, which is closer to the theoretical value of 0.006. This indicates that the lowering of barrier height in the junction depletion region is most likely due to Poole–Frenkel effect. Nevertheless, it should be noted that, out of two leakage current flow mechanisms, viz., interface-controlled current (thermionic emission or tunneling carrier

injection) or bulk-controlled (space charge limited or PFE), at least one mechanism of each class is in effect at the same current level.³⁹ Hence, an exact match of the slope based on any one of the single mechanisms is not expected. It should also be noted here that since the detector did not use any guard ring, the measured leakage current might have contributions from the surface leakage currents.

Considering that the metal contact and the substrate layer constitutes a parallel plate capacitor with the depletion layer as a dielectric medium, the variation of depletion capacitance C as a function of reverse bias voltage could be written as

$$\frac{1}{C^2} = \frac{2}{qA^2\epsilon_0\epsilon_{4H-SiC}N_{eff}}(V + V_{bi}), \quad (6)$$

where N_{eff} is the effective doping concentration in the depletion region and V_{bi} is the built-in potential. The Schottky barrier height can also be calculated from the C - V curves using Eq. (7),

$$\phi_{b(C-V)} = V_{bi} + V_n, \quad (7)$$

where V_n is the potential difference between the Fermi level energy and the bottom of the conduction band in the neutral region of the semiconductor and is given by

$$V_n = kT \ln \frac{N_c}{N_{eff}}, \quad (8)$$

where N_c is the effective density of states in the conduction band of 4H-SiC and is taken equal to $1.6 \times 10^{19} \text{ cm}^{-3}$.⁴⁰ The inset in Fig. 5 shows the variation of the depletion capacitance as a function of reverse bias. It could be seen that the depletion capacitance decreased with the applied reverse bias, which is expected as the depletion width increases with increase in the reverse bias. Figure 5 shows the

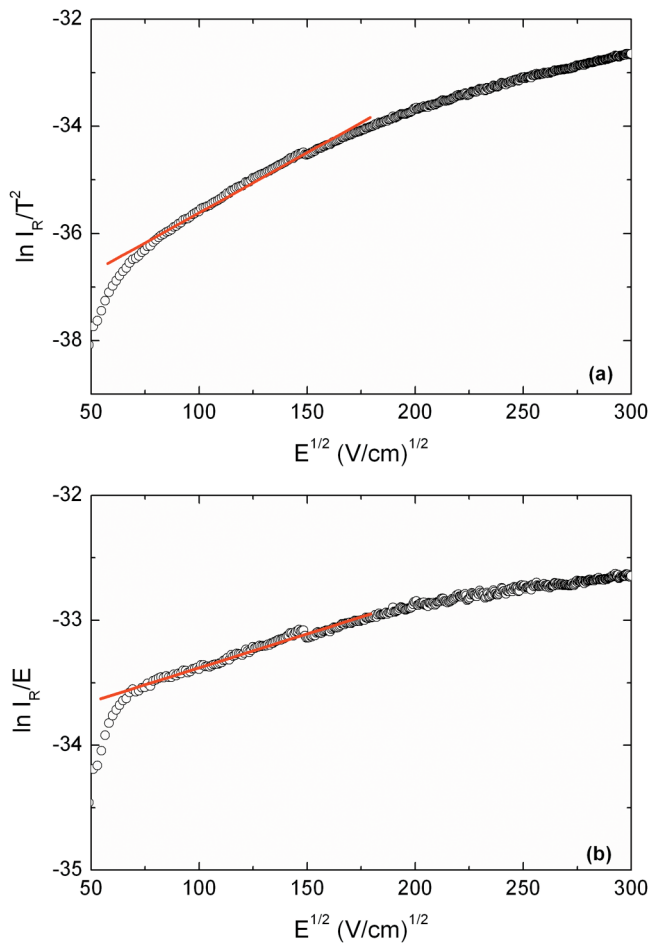


FIG. 4. Electric field dependence of Ni/n-4H-SiC Schottky barrier diode reverse current following the (a) Schottky emission model and (b) Poole–Frenkel emission model. The solid lines are the linear fit and the dots represent the experimental data.

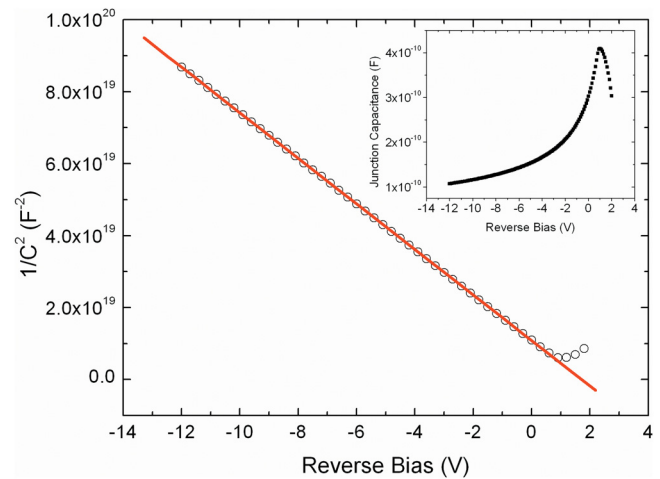


FIG. 5. Mott–Schottky plot derived from the C - V data for a 50 μm Ni/n-4H-SiC Schottky barrier diode. The solid line shows the linear fit to the plot. Inset shows the variation of the depletion capacitance as a function of reverse bias.

Mott-Schottky ($\frac{1}{C^2}$ vs V) plot of the Ni/n-4H-SiC Schottky barrier diode fitted with a straight line following the model provided in Eq. (6). An effective doping concentration of $1.9 \times 10^{14} \text{ cm}^{-3}$ and built-in potential of 1.7 eV was calculated from the fit parameters. The value of V_n was calculated to be 0.3 eV using Eq. (8). The barrier height calculated from the Mott-Schottky plots and Eq. (7) was found to be 2.0 eV, which is higher than that obtained from the I - V measurements. Barrier height obtained from the forward I - V characteristics is generally dominated by the current flow through the low Schottky barrier height locations in a Schottky diode with a spatially inhomogeneous barrier height, which results in a lower surface barrier height. C - V characteristics, on the other hand, give an average value of the barrier height for the whole diode area.^{41,42}

B. Radiation detection measurements

Figure 6 shows a pulse height spectrum obtained from the 50 μm Ni/n-4H-SiC Schottky barrier detector biased at -120 V and exposed to a ^{241}Am alpha source. The inset in Fig. 6 shows that the primary alpha peaks with energies 5388, 5443, and 5486 keV were partially resolved. The three peaks were located at 4389, 4452, and 4515 keV in the calibrated PHS indicating charge loss. The peaks will be henceforth addressed by their original energy. The partially resolved peaks were deconvoluted using Gaussian functions and the fitted curves are shown in the inset of Fig. 6. The 5486 keV peak was well-resolved with a full width at half maximum ($FWHM_{tot}$) of $\sim 37.5 \text{ keV}$, which translates to an energy resolution of 0.8% for 4515 (5486) keV alpha particles. A pulser peak was also acquired along with the alpha spectrum. The $FWHM$ of the pulser peak that gives the overall electronic noise ($FWHM_{elec}$) was found to be 18.3 keV. The intrinsic detector resolution ($FWHM_{det}$) can

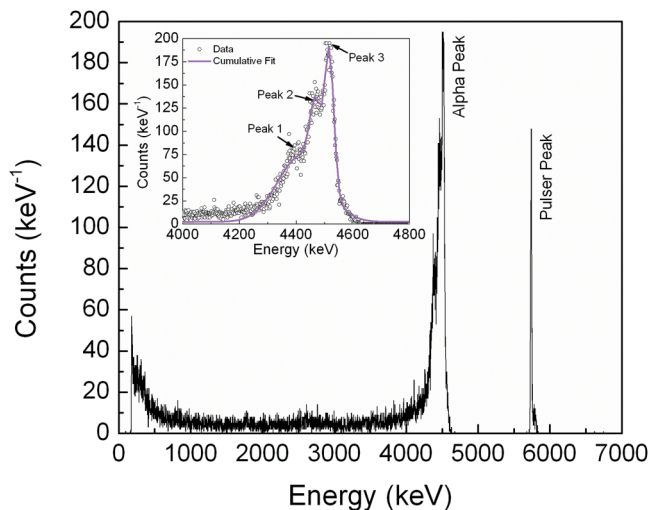


FIG. 6. Pulse height spectrum obtained from a Ni/n-4H-SiC Schottky barrier detector exposed to a ^{241}Am alpha particle source and biased at -120 V . The pulser peak has been shown at the extreme right of the PHS. Inset shows the cumulative overall fit of the alpha peak after a multiple (three) Gaussian functions fit.

then be obtained from the quadrature sum equation given below [Eq. (9)] and was calculated to be 32.7 keV. The above values indicate that the energy resolution of the detector is not limited by the electronic noise (including detector leakage current) of the detection setup in which case it could be assumed that the trap centers are present in the epilayers that degrade the carrier lifetimes,

$$FWHM_{tot}^2 = FWHM_{det}^2 + FWHM_{elec}^2. \quad (9)$$

C. Bias dependence of the SBD performance

Figure 7(a) shows the variation of the centroid of the 5486 keV alpha peak as a function of detector operating bias. The centroid position of the peak is the actual energy sensed by the detector. The figure also includes the variation of the pulser peak centroid, which helps decide if any change observed in the spectral features is due to the detector properties and not due to any unwanted change in the detection electronics. The centroid position of the pulser peak in this case is seen to be stable indicating

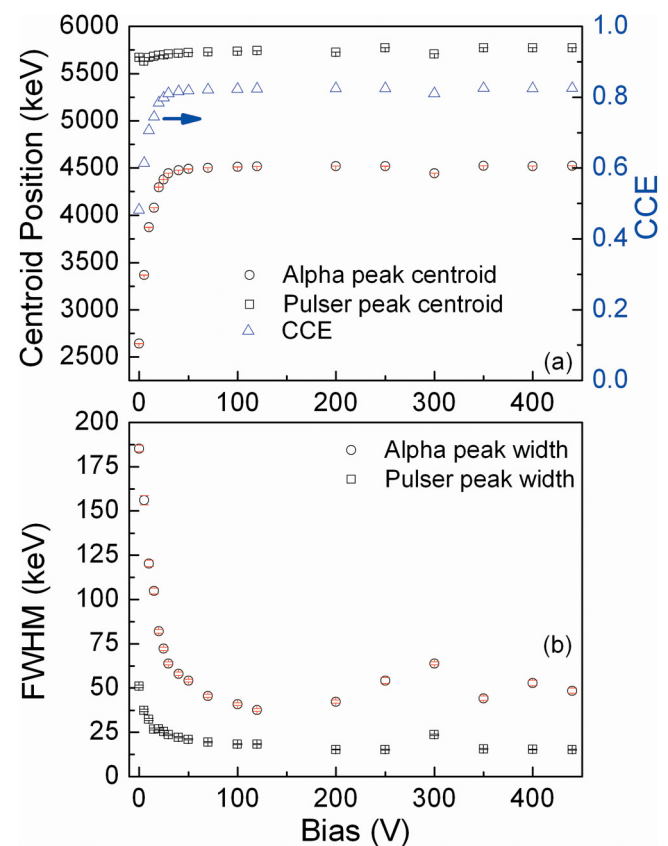


FIG. 7. (a) Variation of peak centroid position as a function of reverse bias voltage for the 5486 keV and the pulser peak. The right-hand axis plots the variation of CCE with bias voltage. (b) Variation of the $FWHM$ of the 5486 keV alpha peak and the pulser peak as a function of bias voltage.

the stability of the electronics. The charge collection efficiency (CCE) defined as the ratio of the energy registered by the detector to the energy emitted by the source has also been plotted in Fig. 7(a). The CCE was calculated as the ratio of the location of the alpha peak (E_{α}) on the MCA (expressed in energy units) and the actual energy emitted by the source (5486 keV). The energy loss at the detector window has not been taken into consideration in the calculation of CCE. The E_{α} value was obtained after calibrating the spectrometer using a precision pulser. Pulses of various known amplitudes (V_{pulser}) from a precision pulser was injected through a calibrated feedthrough capacitor with capacitance C ($=1.95$ pF) to the preamplifier input, and the peak positions of the shaped pulses in the MCA were noted. The material equivalent pulse height of the pulse amplitudes, E_{pulser} , is given by

$$E_{\text{pulser}} = \frac{V_{\text{pulser}} \times \epsilon \times C}{q}, \quad (10)$$

where q is the electronic charge and ϵ is the electron hole-pair creation energy of the detector material taken as 7.8 eV.⁴³ The MCA peak positions were then plotted as a function of E_{pulser} . Assuming a linear behavior of the spectrometer, a linear regression of the data points gives the calibration parameters. The CCE value (~ 0.82) was seen to saturate beyond -50 V. It should be noted here that the calculation of the CCE value did not include the energy loss at the 20 nm thick Ni window or any other dead layer if present.

Figure 7(b) shows the variation of the alpha peak FWHM as a function of the bias voltage. The figure also includes the variation of the pulser peak widths. The FWHM of the alpha peak was found to be relatively higher at lower bias voltages and gradually reducing with increasing bias. Similar variation of the pulser peak width indicates that the reason behind the decrease in the peak width is due to the reduction in the white series noise and the pink noise.⁴⁴ The optimum detector resolution was seen to be reached at -120 V consistent with that observed from the centroid variation. Although the detector resolution was seen to fluctuate slightly beyond -120 V, a similar resolution was obtained for the primary alpha peak at -440 V as well.

D. Deep-level transient spectroscopy (DLTS)

For the DLTS measurements, the diode was biased at a steady-state reverse bias voltage of -2 V. A filling pulse of height 2.0 V with a width of 1 ms was used. After the termination of the filling pulse, the depletion capacitance of the diode relaxes to its equilibrium value by thermally emitting the trapped charges (electrons), resulting in capacitance-transients, which can be expressed as

$$C(t) = C_0 + \Delta C e^{-t/\tau_n}, \quad (11)$$

where C_0 is the depletion capacitance at steady-state reverse bias and ΔC is the change in depletion capacitance within a rate window. The emission rates e_n are found by fitting the capacitance-transients to Eq. (11) for each temperature in the entire scan range and with a ΔC value characterized by the rate window. The emission rate is supposed to vary with the temperature as given in Eq. (12), and hence the capture cross section σ_n and the location of the trap

energy level below the conduction band edge (ΔE) can be obtained from a linear fit of the $\ln e_n$ vs $1/T$ (Arrhenius) plot,⁴⁵

$$e_n = (\sigma_n \langle v_{th} \rangle N_c / g) e^{-\Delta E / kT}. \quad (12)$$

Here, $\langle v_{th} \rangle$ is the mean thermal velocity of electrons and g is the degeneracy of the trap level, which has been considered 1 in the present case. Figure 8(a) shows the DLTS spectra for the Ni/n-4H-SiC epilayer Schottky barrier diode for four correlators used in the temperature range 80–750 K. Three well-defined peaks were observed related to three deep-level defect centers in the given temperature range. Figure 8(b) shows the Arrhenius plot corresponding to the DLTS peaks shown in Fig. 8(a). The concentration of the defects N_t could be found using

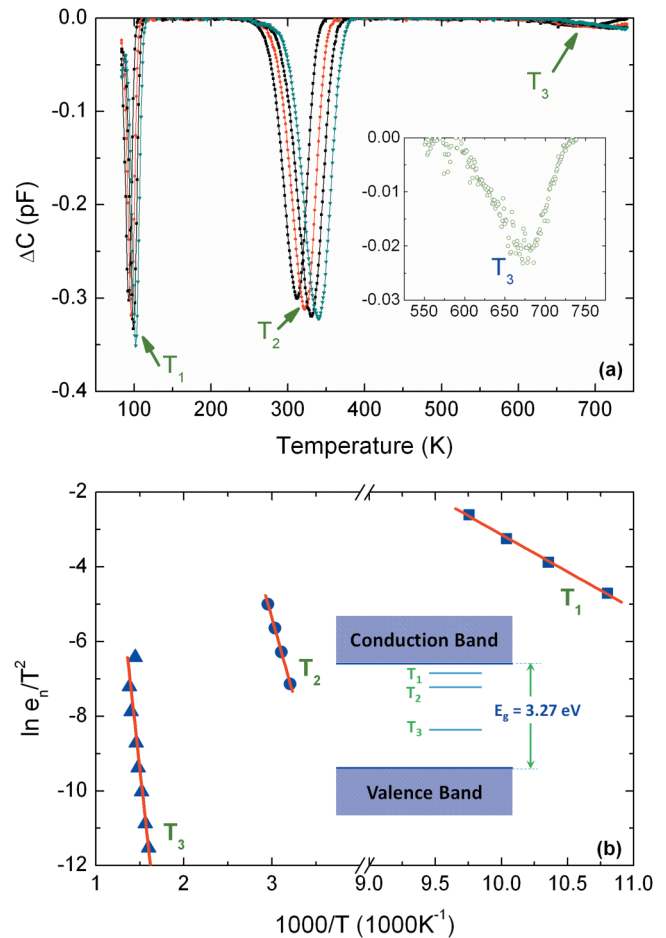


FIG. 8. (a) Deep-level transient spectrum obtained for a Ni/n-4H-SiC epilayer Schottky barrier diode in the temperature range 80–750 K using four correlators with rate windows 0.04, 0.02, 0.2, and 0.4 ms⁻¹ (left to right). The inset shows the zoomed-in peak T_3 for one of the correlators. (b) Arrhenius plots of the three DLTS peaks shown in (a). The solid lines are the linear fit.

TABLE I. Trap parameters obtained from the DLTS measurements of Ni/n-4H-SiC epilayer Schottky barrier diode.

Peak	σ_n cm ²	ΔE eV	N_t cm ⁻³	Possible trap identity
T ₁	5.61×10^{-14}	$E_c - 0.17$	2.03×10^{12}	Ti(c)
T ₂	1.28×10^{-13}	$E_c - 0.73$	2.27×10^{12}	Z _{1/2}
T ₃	1.88×10^{-14}	$E_c - 1.59$	1.76×10^{11}	EH _{6/7}

$$N_t = 2 \left(\frac{\Delta C(0)}{C_0} \right) N_{eff}. \quad (13)$$

Here, $\Delta C(0)$ is the change in depletion capacitance at the end of the filling pulse. The trap parameters calculated from the DLTS spectra are given in Table I. The concentration of the trap centers T₁ and T₂ situated at 0.17 eV and 0.73 eV below the conduction band edge was found to be of the order of 10^{12} cm⁻³, which is an order less than that reported earlier in one of our 50 μ m Ni/n-4H-SiC epilayer SBD, which also incidentally had a higher micropipe density of ~ 15 cm⁻².²⁷ The capture cross sections were also found to be lower by an order of two. Trap center T₁ can be identified as titanium related impurity type defect, which has been assigned to the ionized titanium acceptor Ti³⁺ residing at cubic Si lattice sites and normally designated as Ti(c).^{46–49}

The defect center T₂ has been well-identified as the Z_{1/2} center related to defect complexes involving an equal number of carbon and silicon sites such as silicon and carbon vacancy complexes (V_{Si} + V_C) and antisite complexes (Si_C + C_{Si}) pairs.⁴⁸ Z_{1/2} center has also been established as a carrier lifetime deteriorating defect^{25,47,50,51} and plays a crucial role in defining the energy resolution of the detectors. The defect center T₃, situated 1.59 eV below the conduction band edge, has been identified as carbon vacancies or carbon-silicon di-vacancies (EH_{6/7}).⁵² EH_{6/7} was not observed in our previously fabricated 50 μ m epilayer detectors.²² However, we did observe this type of defect in our ultrahigh resolution 20 μ m epilayer detector fabricated earlier.^{15,26} It was observed there that the 20 μ m epilayer detector, which exhibited the highest resolution, has the lowest EH_{6/7} trap concentration of $\sim 10^{11}$ cm⁻³ similar to the present sample. It should also be noted that apart from the concentration of the defects, their capture cross sections also define how effective a defect would be to influence the electrical properties of the detector. The capture cross section of a defect is related to its charge state. It was observed in our previous study²⁶ that the energy resolution of the detectors with the lower capture cross section of EH_{6/7} performed much better even though they have equal concentration of the defect. The present sample has a capture cross section of the EH_{6/7} defect, which is toward the higher side.

IV. CONCLUSION

Schottky barrier detectors have been fabricated from 50 μ m thick 4H-SiC n-type epitaxial layers grown on highly conducting 4H-SiC substrates. The substrates, 100 mm in diameter and 350 μ m thick, were 8° offcut toward the $\langle 11\bar{2}0 \rangle$ direction. The epilayers were grown on the (1000) plane (Si face). The epilayers were characterized

with a micropipe density less than 1/cm². Square shaped (8 × 8 cm²) samples were diced from the parent wafer and Schottky contacts were achieved by depositing 20 nm thin circular Ni contacts on the epilayer surface with a detector area of 11 mm². The *I*-*V* characteristics revealed the formation of Schottky barrier with a barrier height of 1.54 eV, and an ideality factor of 1.5 was obtained using a thermionic emission model applied to the forward *I*-*V* characteristic. The *C*-*V* measurements revealed the effective doping concentration in the epilayer to be 1.9×10^{14} cm⁻³. It was calculated that for the given effective doping concentration, a bias voltage of ~ 440 V was necessary to obtain a full-depletion condition. The reverse *I*-*V* characteristics revealed a leakage current of 0.6 nA at a reverse bias of -450 V ensuring that the Schottky diode could be used as a radiation detector at -450 V bias or even above with a high-energy resolution. It was also found that the reverse current flow mechanism through the detector is mostly bulk-controlled through the Poole-Frenkel effect. The detector was tested for radiation detection properties by exposing it to a ²⁴¹Am alpha particle source. All the three primary alpha peaks emitted by the ²⁴¹Am could be identified in the PHS. The 5486 keV alpha peak showed an energy resolution of 0.8% when the detector was biased at -120 V. The performance of the detector remained unaltered up to a bias voltage of -440 V at which the detector was fully depleted to 50 μ m. The extra-stability of the detector has been attributed to the low leakage current at such high voltages. Leakage currents are mostly controlled by the surface barrier properties and the electrically active charge trapping centers. To investigate the defect levels, capacitance-DLTS studies revealed three defect levels in the temperature scan range of 80–750 K and were identified as Ti(c), Z_{1/2}, and EH_{6/7} defects. The Z_{1/2} defect is related to Si and C vacancy complex or antisite complex sites and EH_{6/7} defects are believed to be carbon vacancies or carbon-silicon di-vacancies, and both are known to limit the energy resolution of detectors significantly. Ti(c) is a relatively shallow defect and is generally assigned to the Ti impurities at cubic silicon sites. The defect concentrations were calculated from the DLTS spectra to be of the order of 10^{12} cm⁻³. The Z_{1/2} and EH_{6/7} defects were believed to limit the energy resolution of the fabricated detectors.

ACKNOWLEDGMENTS

This work was supported by the DOE Office of Nuclear Energy's Nuclear Energy University Program (NEUP) (Grant Nos. DE-AC07-051D14517 and DE-NE0008662). The work was also supported in part by the Advanced Support Program for Innovative Research Excellence-I (ASPIRE-I) (Grant No. 15530-E404) and Support to Promote Advancement of Research and Creativity (SPARC) (Grant No. 15530-E422) of the University of South Carolina (UofSC), Columbia, USA.

DATA AVAILABILITY

The data that support the findings of this study are available from the corresponding author upon reasonable request.

REFERENCES

- K. C. Mandal, J. W. Kleppinger, and S. K. Chaudhuri, *Micromachines* **11**, 254 (2020).
- R. Schifano, A. Vinattieri, M. Bruzzi, S. Miglio, S. Logomarsino, S. Sciortino, and F. Nava, *J. Appl. Phys.* **97**, 103539 (2005).

- ³G. Puglisi and D. Bertuccio, *Micromachines* **10**, 835 (2019).
- ⁴K. V. Nguyen, M. A. Mannan, and K. C. Mandal, *IEEE Trans. Nucl. Sci.* **62**, 3199 (2015).
- ⁵F. H. Ruddy, A. R. Dullo, J. G. Seidel, M. K. Das, S. Ryu, and A. K. Agarwal, *IEEE Trans. Nucl. Sci.* **53**, 1666 (2006).
- ⁶F. H. Ruddy, J. G. Seidel, H. Chen, A. R. Dullo, and S. Ryu, *IEEE Trans. Nucl. Sci.* **53**, 1713 (2006).
- ⁷G. Bertuccio, R. Casiraghi, A. Cetronio, C. Lanzieri, and F. Nava, *Nucl. Instrum. Methods Phys. Res. A* **522**, 413 (2004).
- ⁸S. O. Kasap, *Optoelectronics Photonics: Principles Practices* (Pearson Education Limited, 2009).
- ⁹G. Lucas and L. Pizzagalli, *Nucl. Instrum. Methods Phys. Res. A* **229**, 359 (2005).
- ¹⁰P. G. Neudeck, D. J. Spry, L. Chen, N. F. Prokop, and M. J. Krasowski, *IEEE Electron Device Lett.* **38**, 1082 (2017).
- ¹¹J. Wu, Y. Jiang, M. Li, L. Zeng, J. Li, H. Gao, D. Zou, Z. Bai, C. Ye, W. Liang, S. Dai, Y. Lu, R. Rong, J. Du, and X. Fan, *Rev. Sci. Instrum.* **88**, 083301 (2017).
- ¹²L. Torrisi, G. Foti, L. Giuffrida, D. Puglisi, J. Wolowski, J. Badziak, P. Parys, M. Rosinski, D. Margarone, J. Krasa, A. Velyhan, and U. Ullschmied, *J. Appl. Phys.* **105**, 123304 (2009).
- ¹³G. Bertuccio, D. Puglisi, L. Torrisi, and C. Lanzieri, *Appl. Surf. Sci.* **272**, 128 (2013).
- ¹⁴F. Nava, P. Vanni, M. Bruzzi, S. Lagomarsino, S. Sciortino, G. Wagner, and C. Lanzieri, *IEEE Trans. Nucl. Sci.* **51**, 238 (2001).
- ¹⁵S. K. Chaudhuri, K. J. Zavalla, and K. C. Mandal, *Nucl. Instrum. Methods Phys. Res. A* **728**, 97 (2013).
- ¹⁶G. Bertuccio, R. Casiraghi, and F. Nava, *IEEE Trans. Nucl. Sci.* **48**, 232 (2001).
- ¹⁷G. Bertuccio, D. Puglisi, A. Pullia, and C. Lanzieri, *IEEE Trans. Nucl. Sci.* **60**, 1436 (2013).
- ¹⁸K. C. Mandal, P. G. Muzykov, S. K. Chaudhuri, and J. R. Terry, *IEEE Trans. Nucl. Sci.* **60**, 2888 (2013).
- ¹⁹K. C. Mandal, R. M. Krishna, P. G. Muzykov, S. Das, and T. S. Sudarshan, *IEEE Trans. Nucl. Sci.* **58**, 1992 (2011).
- ²⁰X. R. Huang, M. Dudley, W. M. Vetter, W. Huang, W. Si, and J. C. H. Carter, *J. Appl. Cryst.* **32**, 516 (1999).
- ²¹R. A. Stein, P. Lanig, and S. Leibenzeder, *Mater. Sci. Eng. B* **11**, 69 (1992).
- ²²J. J. Sumakeris, J. R. Jenny, and A. R. Powell, *MRS Bull.* **30**, 280 (2005).
- ²³P. G. Neudeck, *Mater. Sci. Forum* **338–342**, 1161 (1999).
- ²⁴H. Lendenmann, F. Dahlquist, N. Johansson, R. Söderholm, P. A. Nilsson, P. Bergman, and P. Skytt, *Mater. Sci. Forum* **353–356**, 727 (2001).
- ²⁵T. Kimoto, K. Danno, and J. Suda, *Phys. Status Solidi B* **245**, 1327 (2008).
- ²⁶K. C. Mandal, S. K. Chaudhuri, K. V. Nguyen, and M. A. Mannan, *IEEE Trans. Nucl. Sci.* **61**, 2338 (2014).
- ²⁷M. A. Mannan, S. K. Chaudhuri, K. V. Nguyen, and K. C. Mandal, *J. Appl. Phys.* **115**, 224504 (2014).
- ²⁸J. Li, C. Meng, L. Yu, Y. Li, F. Yan, P. Han, and X. Ji, *Micromachines* **11**, 609 (2020).
- ²⁹W. Chen and M. A. Capano, *J. Appl. Phys.* **98**, 114907 (2005).
- ³⁰W. Kern, *J. Electrochem. Soc.* **137**, 1887 (1990).
- ³¹S. K. Chaudhuri, K. J. Zavalla, and K. C. Mandal, *Appl. Phys. Lett.* **102**, 031109 (2013).
- ³²B. Zafko, F. Dubecký, A. Šagátová, K. Sedláčková, and L. Ryč, *J. Instrum.* **10**, C04009 (2015).
- ³³G. Bertuccio, S. Caccia, R. Casiraghi, and C. Lanzieri, *IEEE Trans. Nucl. Sci.* **53**, 2421 (2006).
- ³⁴A. Poyai, E. Simoen, C. Claeys, A. Czerwinski, and E. Gaubas, *Appl. Phys. Lett.* **78**, 1997 (2001).
- ³⁵T. Takahashi, T. Mitani, Y. Kobayashi, M. Kouda, G. Sato, S. Watanabe, K. Nakazawa, Y. Okada, M. Funaki, R. Ohno, and K. Mori, *IEEE Trans. Nucl. Sci.* **49**, 1297 (2002).
- ³⁶H. A. Bethe, MIT Radiation Laboratory Report 43-12 (1942).
- ³⁷E. Rhoderick, *IEEE Proc.* **129**, 1 (1982).
- ³⁸S. M. Sze and M. K. Lee, *Semiconductor Devices*, 3rd ed. (John Wiley & Sons, Inc., 2012).
- ³⁹H. Schroeder, *J. Appl. Phys.* **117**, 215103 (2015).
- ⁴⁰Y. Goldberg, M. E. Levinstein, and S. L. Rumyantsev, *Properties of Advanced Semiconductor Materials GaN, AlN, InN, BN, SiC, SiGe* (John Wiley & Sons, Inc., New York, 2001), p. 99.
- ⁴¹R. T. Tung, *Phys. Rev. B* **45**, 13509 (1992).
- ⁴²M. Jang, Y. Kim, J. Shin, and S. Lee, *IEEE Electron Device Lett.* **26**, 354 (2005).
- ⁴³G. Bertuccio and R. Casiraghi, *IEEE Trans. Nucl. Sci.* **50**, 175 (2003).
- ⁴⁴G. Bertuccio and A. Pullia, *Rev. Sci. Instrum.* **64**, 3294 (1993).
- ⁴⁵D. V. Lang, *J. Appl. Phys.* **45**, 3023 (1974).
- ⁴⁶T. Dalibor, G. Pensl, N. Nordell, and A. Schöner, *Phys. Rev. B* **55**, 13618 (1997).
- ⁴⁷Ł. Gelczuk, M. Dąbrowska-Szata, M. Sochacki, and J. Szmidi, *Solid State Electron.* **94**, 56 (2014).
- ⁴⁸J. Zhang, L. Storasta, J. P. Bergman, N. T. Son, and E. Janzén, *J. Appl. Phys.* **93**, 4708 (2003).
- ⁴⁹A. Castaldini, A. Cavallini, L. Polenta, F. Nava, C. Canali, and C. Lanzieri, *Appl. Surf. Sci.* **187**, 248 (2002).
- ⁵⁰T. Tawara, H. Tsuchida, S. Izumi, I. Kamata, and K. Izumi, *Mater. Sci. Forum* **457–460**, 565 (2004).
- ⁵¹P. B. Klein, B. V. Shanabrook, S. W. Huh, A. Y. Polyakov, M. Skowronski, J. J. Sumakeris, and M. J. O'Loughlin, *Appl. Phys. Lett.* **88**, 052110 (2006).
- ⁵²K. Danno, T. Kimoto, and H. Matsunami, *Appl. Phys. Lett.* **86**, 122104 (2005).